Brückner, M.Z.M., et al., 2024, Bank strength variability and its impact on the system-scale morphodynamics of the upper Amazon River in Brazil: Geology, https://doi.org/10.1130/G51862.1

# Supplemental Material

Measurements, GIS data, and Landsat, CORONA, and MBES imagery, along with a detailed description of the methodology.

# Bank strength variability and its impact on the system-scale morphodynamics of the upper Amazon River in Brazil - Supplemental Material

**Muriel Z.M. Brückner, Rolf E. Aalto, Jim ~~L.~~ Best, Renato Paes de Almeida, Andrew P. Nicholas, Philip J. Ashworth, Marco Ianniruberto**

**Content**



## 1) Bank strength measurements and processing

1.1) Description of the shear vane and the cohesion strength meter

The hand-held shear vane (Figure S1A) was designed for soft homogenous clays (Jafari et al., 2019) and records the axial strength of the top layer of the test material to a depth dependent on the length of the blade (He et al., 2018). After insertion into the cohesive material, the blade is rotated at a constant angular speed until the material fails. The undrained shear strength can then be directly extracted based on the torque and dimensions of the shear vane. For each sample, 6-12 tests were conducted to characterize the spatial variability of shear strength, assuming that the material penetrated by the vanes was homogeneous and isotropic (He et al., 2018). For our field analysis, we tested 3 different shear vane devices across a range of sediments and sedimentary rocks, exploring the repeatability of each device and honing our techniques. Following these trials, we ultimately focused our reported data collection and analysis on results only from the large, professional model that we determined to provide the best consistency for the study exposures (Pilcon Shear Vane; New Zealand Geotechnical Society, 2001).

The Cohesive Strength Meter (CSM; Figure S1B) records the critical shear strength for erosion based on a jet-pressure test (Tolhurst et al., 1999; Vardy et al., 2007). The CSM test chamber is set onto the flat surface of the deposits and fires a perpendicular jet of water in short pulses at the sediment surface. By increasing the force of the jet in 0.05 Pa increments, the point of incipient scour can be identified through optical sensors that record the transmission of infra-red light through the water. Bed erosion is determined by the reduction in transmission in the test chamber due to resuspended sediment. Herein, we defined the critical transmission point at 90% of the initial transmission (Widdows et al., 2007). The pressure recorded by the CSM can be used to calculate the critical shear stress at the onset of erosion based on the calibration provided by Tolhurst et al. (1999):

$$\tau_{cr} = 66.6734 * \left(1 - e^{-\frac{P}{310.09433}}\right) - 195.27552 * (1 - e^{-\frac{P}{1622.56738}})$$

where $P$ [kPa] is jet pressure and $\tau_{cr}$ [N/m2] is equivalent to the horizontal erosion shear stress for jet pressures up to 30 psi. Figure S2 shows an example of the calculated critical shear stress and resulting decrease in transmission. While these results are useful to parameterize river erodibility in models, they are only representative of dry surface sediments that exclude the effects of vegetation. Mass failure due to bank collapse and cohesivity from roots are not included in the results.

Our CSM (Mark III) had been recently serviced by the manufacturer and retested by us in the UK prior to the fieldwork. Because it was not possible to fill high pressure SCUBA air tanks near our remote field location, we devised a bespoke air pressure source that met the specific requirements of the CSM, combining several locally sourced pressure tanks with custom connectors brought from the UK, and recharged daily with a portable air compressor. Because the CSM measures the input pressure and precisely controls the output pressure, we were able to ensure that the pressure supplied was always to specification.

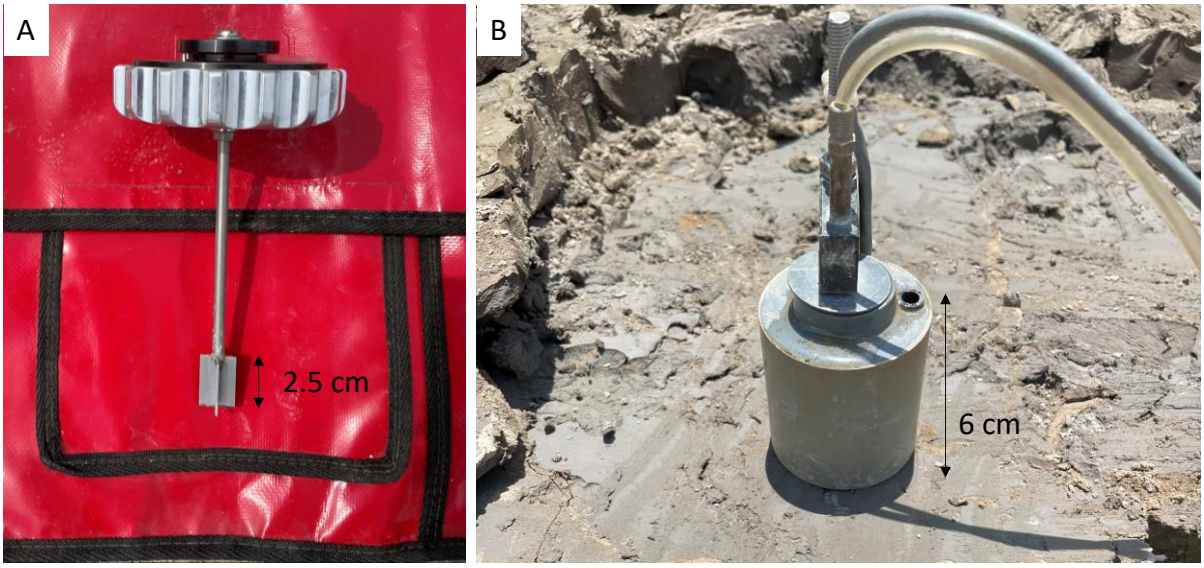


**Figure S1.** A) Pilcon shear vane; B) test chamber of the Cohesion Strength Meter.

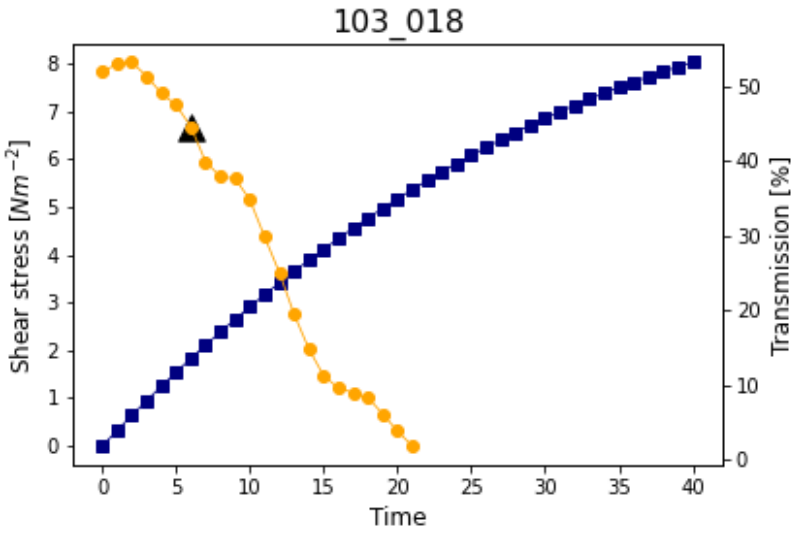

**Figure S2.** Example of parameters recorded by the CSM: over time, a step-wise increase in shear stress (blue line) results in a reduction in transmission (yellow line). Black triangle indicates the threshold for resuspension at a drop to 90% of the initial transmission value.

### 1.2) Statistical analysis

For the measurements, we carried out a t-test for the means of two independent samples using the Python SciPy package. The test shows that the two samples are drawn from the same distribution when the null-hypothesis is accepted. For the shear vane measurements, we rejected the null-hypothesis ($p= 5*10^{-7}$), whereas the null-hypothesis was accepted for the CSM measurements (p-value = 0.26).

## 2) Preparation of the satellite imagery extracted from Google Earth Engine

For the reach-scale analysis, we downloaded composite images for 1984-88 and 2019-23 from Google Earth Engine using the code provided by Boothroyd et al. (2020), which computes binary maps of wet and dry areas from Landsat imagery (30 m resolution) based on cloud-free images. The binary maps were processed in ESRI ArcMap to remove small-scale channels and floodplain lakes. We selected three reaches that transition from freely meandering (reach I) to partially-constrained (reach II) with reach III being partially-constrained at a confluence with a secondary channel. Partially-constrained was defined based on our field observations and in comparison with FABDEM (Hawker et al., 2022). When the active channel was located close to PCCS in parts of the reach, the channel was defined as partially-constrained. Figure S3 shows the workflow for the data analysis using ESRI ArcMap and MATLAB. We segmented the cleaned binary maps into segments of 20-km reaches (reach I and II) and 10-km reaches (reach III) based on the river kilometers provided by the Brazilian Navy. Each segment was exported at a 20 m grid cell resolution and imported into MATLAB 2023. The wet channel mask was used to computed centerlines, mean active channel width and channel belt width, and sinuosity using the rivMAP toolbox (Schwenk et al., 2017) based on skeletonization (see Table S1). We used the centerlines to separate the channel into north and south banks. In addition, we computed channel sinuosity for the years 2019-23 by dividing centerline length by reach length measured in ArcGIS Pro. The binary maps for channel and bars were subtracted separately to derive maps of areal change for channels and bars. We averaged erosion area along each bank and computed net deposition area along each segment defined as the mean net channel change from classified water to land. We divided the area change by the 30 years between the two time periods and the segment length to derive mean erosion and deposition rates. Net deposition was defined as all areas that experienced deposition minus any eroded areas associated with the bars. This allowed us to compare large-scale lateral movement of the two study sites with the locations of observed outcrops along the south bank.

Table S1: Channel width including bars (channel belt) and active channel width for the three reaches obtained from the rivMAP toolbox for 2019-2023 (Schwenk et al., 2017). M: main channel; S: secondary channel.

| Reach | Mean channel belt width [km] | Mean active channel width [km] |
|---|---|---|
| I | 4.66 | 2.69 |
| II | 3.77 | 2.65 |

| | | |
|---|---|---|
| III (M \| S) | 2.96 \| 1.87 | 2.64 \| 1.24 |

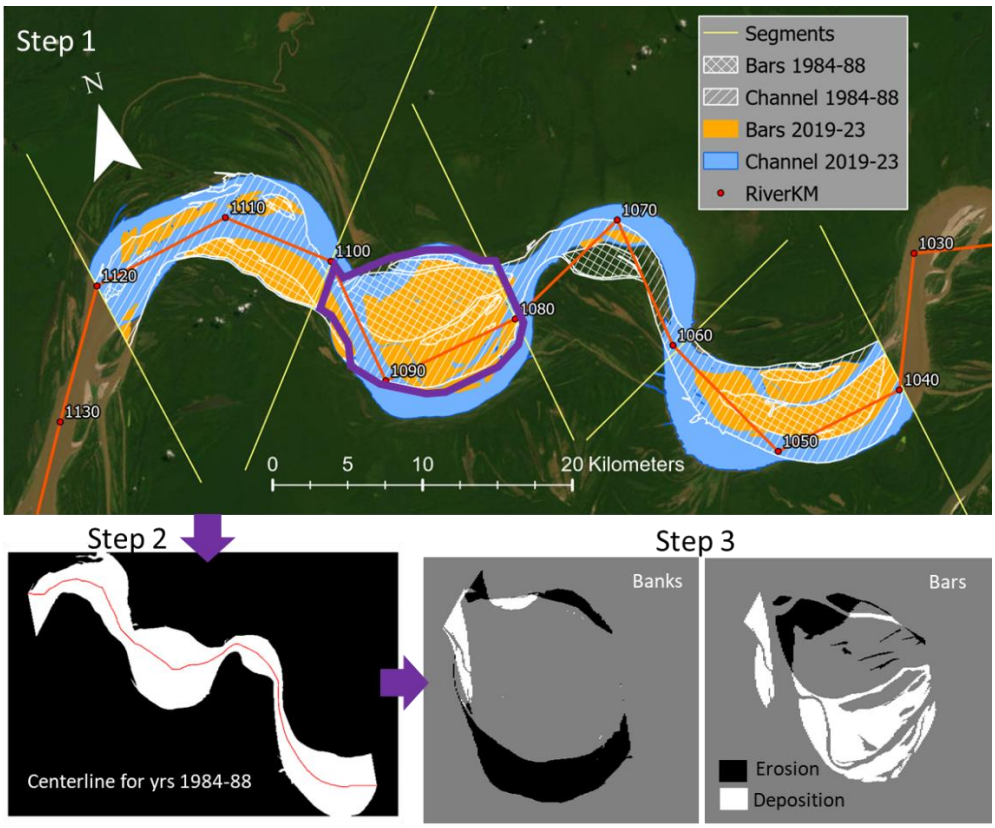


**Figure S3.** Workflow for the processing of the extracted binary maps from Google Earth Engine. Step 1: Division into 10- or 20-km segments based on perpendicular lines along river kilometers (here for river km 1040-1120). Step 2: Extraction of centerlines using the water mask for 1984-88. Step 3: Subtracting 2019-23 and 1984-88 to obtain new water and new land masks along each bank and bars that were classified as erosional and depositional. The centerline was used to separate the left and right banks and compute sinuosity for each segment.

## 3) GIS analysis of the attachment and migration rate for the 1,600 km of the Solimões River

3.1) Classification of bank association to higher terraces from FABDEM.

Resistant terraces were defined through extensive GIS and image analysis through two visual procedures:

1) Sharply defined elevation differences from FABDEM (Hawker et al., 2022) between the 10-15 m high terraces and Holocene floodplain (see Figure S4A). Most locations met these criteria.

2) Assessment of locations with lower terraces (2-5 m height above the modern floodplain), mainly in the downstream reaches, to further verify these as terraces by using high resolution imagery (ArcPro and Google Earth). Specifically, we identified extensive incisional features that indicate that the Holocene channel has not reworked those older sediments (areas marked with 'I' in Figure S4B). These lower terraces are incised alluvial deposits from higher stages of the Pleistocene river, and contain

dissected fluvial features such as levees, channel remnants, oxbow lakes and point bar ridges (Toivonen et al., 2007).

Channel reach (10 river km (rkm)) length was determined from the navigational charts, and considered associated with resistant Pleistocene terraces when the distance from the closest channel bank to the defined resistant terrace was less than the mean channel width for that location, as determined from a best fit regression (Figure S5). The distance measurements were made at the reach midpoint for the first year of the migration analysis (1984), as illustrated in Figure S4A (here all reaches are classified as disassociated).

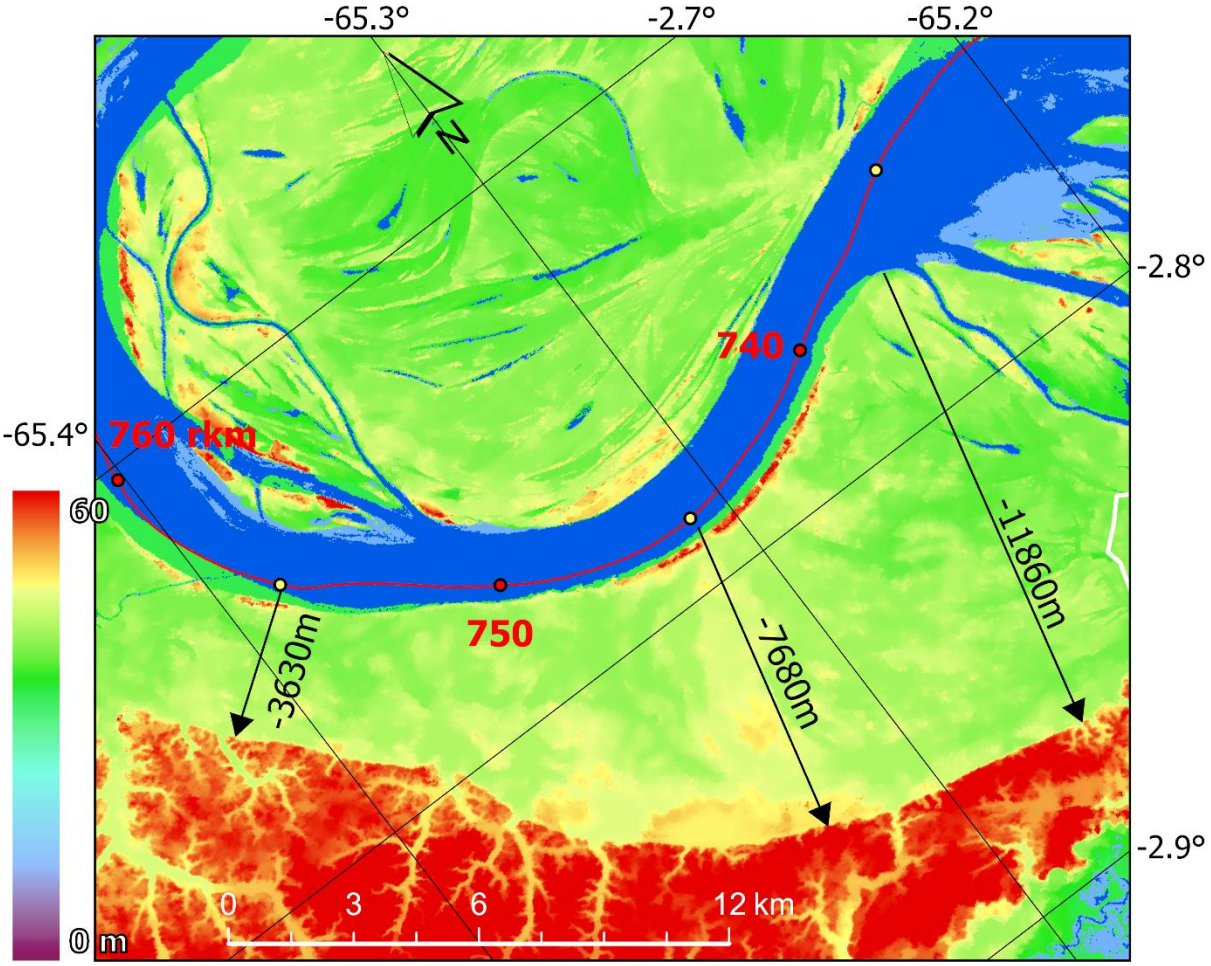


**Figure S4A.** Example reach of middle Solimões River around river kilometer (rkm) 760, with Brazilian Navy rkm points in red and reach midpoints in yellow, as determined from digitization of the 1998 channel centerline. Background map is FABDEM elevations, illustrating the sharp rise in topography to the high, incised terraces, seen as cliffs in the field. The 1984 channel position, as reported by GSWE, is layered over the FABDEM raster in blue, with dark and light blue representing permanent and seasonal inundation, respectively. In this example, distance is measured from the edge of the 1984 channel to the start of the terrace (for the database, distances from the right bank are measured as negative). All such midpoint distances were measured for a range of years, with the initial 1984 measurement used for the analyses presented herein.

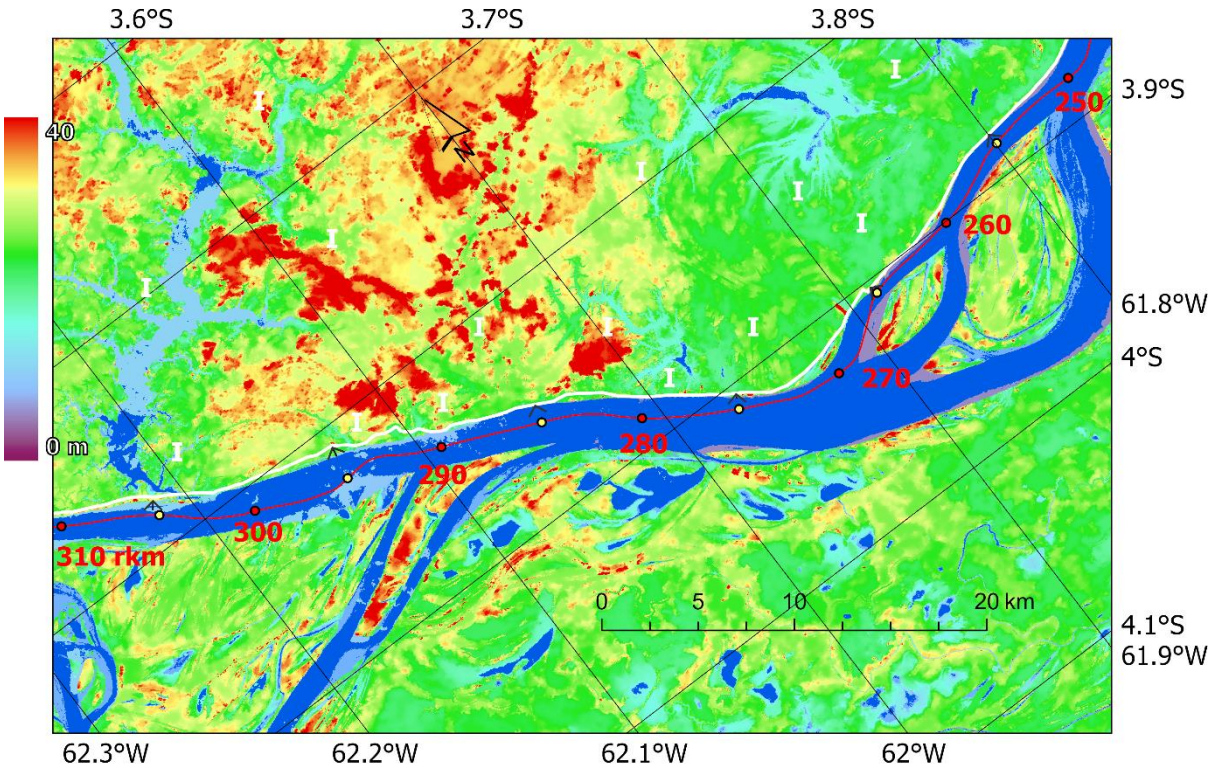


**Figure S4B.** Example reach of middle Solimões River around river kilometer 310, illustrating the lower dissected terraces close to Manaus, with map features similar to Fig. S4A. In this region, the terrace north of the left bank has extensive signs of dissection, unlike the slightly lower floodplain to the south. Multiple incision features, some denoted with a white "I", using both FABDEM and high-resolution imagery were used to classify everything north of the white line as pre-Holocene in age. Distances were measured as in Fig. S4A, but in all cases the river is within a few hundred meters of the older surface to the north, meaning all cases were defined as 'associated'.

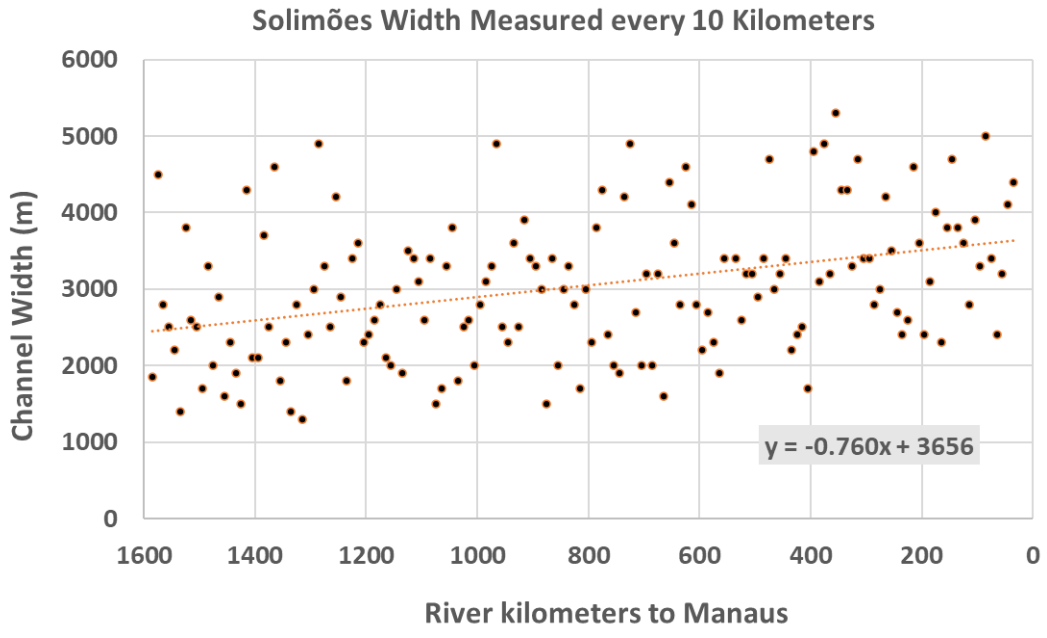


**Figure S5.** Determination of mean channel widths (in meters) from a best-fit regression based on the 1998 Brazilian navigational maps. At the midpoint of each navigational 10 river kilometer (rkm) reach, we measured

the total width, counting across all threads if there were multiple channels at this location. While there is considerable variability, there is also a clear trend of widening downstream towards Manaus (located at rkm 0).

For the present paper, we use a simple definition of channel-terrace 'association', considering all locations closer than one channel width (defined locally according to Figure S5) to be close enough to the terrace to interact with more resistant PCCS bank materials. We acknowledge that there are numerous factors, such as variations in channel width and curvature, bank slope and secondary currents, that determine how these channel-PCCS interactions affect larger scale migration behavior over a range of spatial and temporal scales. The simple approach adopted herein is a first method to assess these relationships, and allow future development of additional metrics based on additional field and GIS data. Note that the bank erosion and deposition rates are limited by the pixel sizes of 30 m. However, these limitations are considered be minor compared with the large width of the Solimões River.

### 3.2) Determining erosion and deposition from Global Water Surface Explorer (GWSE, Pekel et al., 2016) data

For the system-scale analysis, we digitized polygons of approximately 10-km length by creating intervals between the 10 rkm points provided by the Brazilian Navy (note that the official 10-km navigations points are not spaced at exactly 10 km, even for the 1998 chart year, and thus we corrected all of our analyses to the actual segment lengths). Polygons were drawn manually for each river bank (right and left), paying careful attention to the 1984-2021 GWSE change product in order to characterize specifically bank migration over the 37-year time interval. Examples are given here in Figures S6A and S6B, which are co-located with Figures S4A and S4B to facilitate comparisons for these locations. All results of this analysis are given in the accompanying spreadsheets.

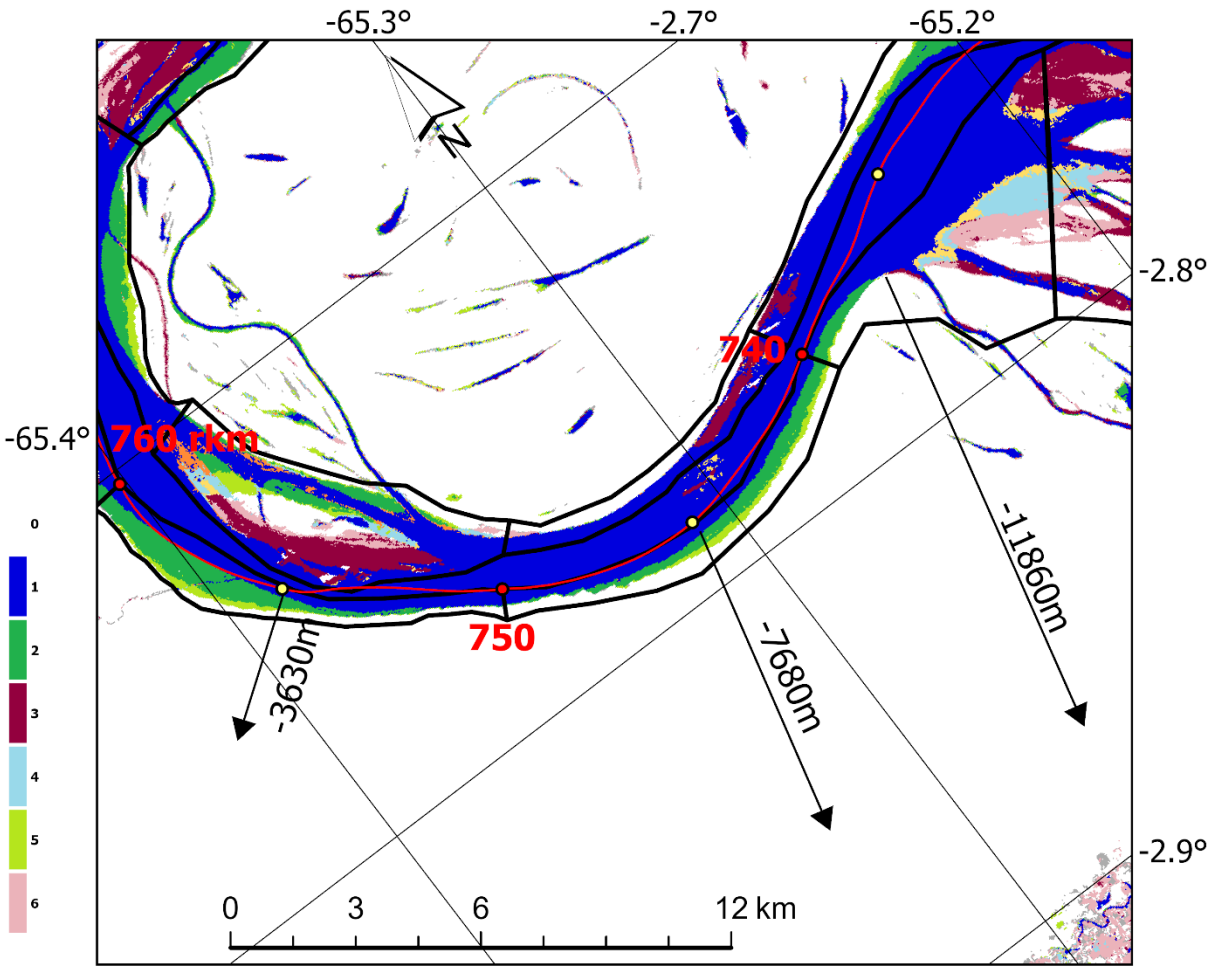


**Figure S6A.** Figure collocated with Fig. S4A illustrating channel movement between 1984 and 2021, according to the GSWE database. In this figure white (0) represents floodplains with no change and blue (1) represents permanent water. Dark green (2) represents permanent new channel and light green (5) represents seasonally flooded new channel, whereas red (3) represents permanent new deposition and light red (6) represents seasonally inundated new deposition. Black polygons for each bank were drawn manually for each 10 river km reach, as defined by Brazilian navigational charts, to fully capture bank movement while minimizing account of floodplain change not related to migration over the period of study.

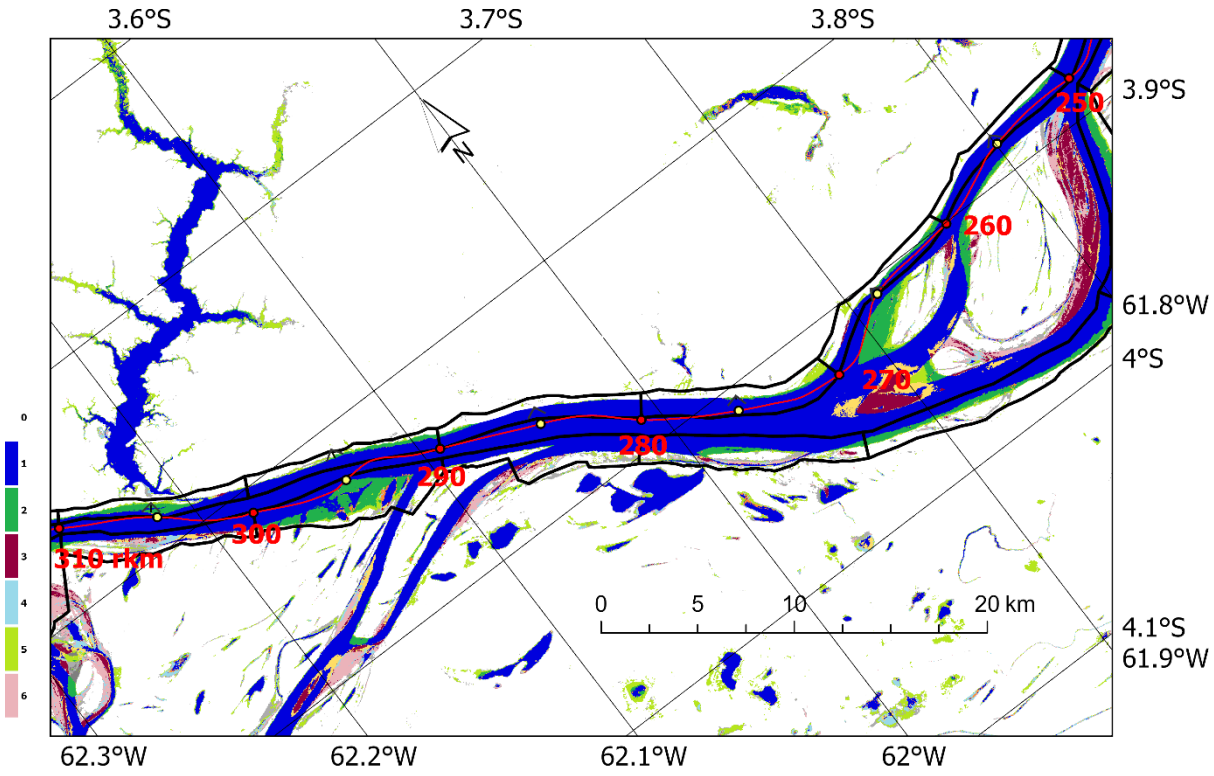


**Figure S6B.** Figure collocated with Fig. S4B, illustrating channel movement between 1984 and 2021, according to the GSWE database. White (0) represents floodplains with no change and blue (1) represents permanent water. Dark green (2) represents permanent new channel and light green (5) represents seasonally flooded new channel, whereas red (3) represents permanent new deposition and light red (6) represents seasonally inundated new deposition.

To minimize accounting for changes in inundated area unrelated to channel migration, we used the following criteria: 1) the river side of the polygon is drawn in permanent water (GSWE zone 1) that does not include islands or mid-channel bars that are separated by more than ~1/10 channel width from the bank in 1984; 2) the floodplain side of the polygon is drawn on permanent floodplain (GSWE zone 0), and digitized deliberately to minimize the accounting of off-channel water bodies, as these may fill in over time; 3) in the few places where bank migration was fast enough that both erosion and deposition had occurred in a single location during the 37 year study period, accounting was also possible such that this complexity was accounted for in the erosion and deposition metrics for the 1984-2021 study interval (there are additional GSWE classes not depicted here).

Following this digitization, for each bank polygon we measured erosion and deposition area between 1984 and 2021 based on the GWSE. Net bank erosion were areas classified as ‘new permanent’ (zone 2) and ‘new seasonal’ (zone 5) by the GWSE, whereas net deposition corresponded to ‘lost permanent’ (zone 3) and ‘lost seasonal’ (zone 6). The net area of both was then divided by the measured reach length (~10km, but varies) and by 37 years to derive annual erosion and deposition distance of both bank sides of each study reach. Note that mid-channel bars or islands were not included in the large-scale analysis, because for this paper we are intentionally only tracking the movement of the bounding channel banks, with reference to their proximity to terraces of PCCS material.

3.3) Statistical analysis

We assessed the two distributions using a two-sample Kolmogorov-Smirnov test for goodness of fit with a 95% confidence interval. The test reveals that the two samples are drawn from the same distribution when the null-hypothesis is accepted. We used the SciPy python package to compare erosion and deposition distribution between the two samples (associated, disassociated). P-values were well below the significant p-value of 0.05, leading to the rejection of the null-hypothesis (erosion: p-value = $6 * 10^{-6}$; deposition: p-value = $6 * 10^{-4}$).

**4) Multi-beam echo sounder and Side-Scan Sonar analysis**

4.1 Multi-Beam Echo Sounder (MBES) data

RuralTech (ruraltech.com.br) completed a MBES survey of key locations throughout our study area. MBES surveys were conducted using a Teledyne Reson SeaBat 7125 that was bow mounted on a dedicated survey vessel with precise DGPS geolocation and Applanix inertial motion unit (IMU) to account for boat motion. The Reson 7125 is a dual 200/400 kHz system, with the 400 kHz forming 512, 0.5° beams in equidistant mode covering a 128° swath, and providing a depth resolution of *c.* 5mm. The raw point cloud data were post processed by RuralTech to remove artifacts using the following procedures.

First, the calibration of the data was enhanced to improve data accuracy and reliability, and the data were then filtered using three steps: a) Detection Quality: Data were for detection quality to eliminate any potential inaccuracies; b) Statistics: A thorough statistical analysis was conducted to identify and rectify any anomalies; c) Flying Objects: The data were screened for any flying object interference and removed accordingly. In addition, manual filtering was undertaken to remove any obvious anomalous points.

RuralTech utilized a bespoke processing routine, GGMatch, to post process the multibeam bathymetry and trajectory data, and compute micro corrections for the trajectory data. The principle of GGMatch is similar to traditional 'Patch-Test' techniques, by which the acquired point cloud data, together with trajectory data (X, Y, Z, Roll, Pitch, Heading), are analyzed to identify the root cause of systematic errors in the point cloud data. This automated process was used to enhance the MBES data and provide a variety of quality control information, such as correction rasters, standard deviations, residual errors, and boresight calibration results. The data output comprises adjusted trajectory files and corrected bathymetric point cloud files for data comparison against source data. GGMatch uses an automatic strip alignment procedure, using sensor trajectory and overlapping swath bathymetry data containing overlapping riverbed topography, and corrects for both relative and absolute geometric errors. This allows the processing to effectively reduce discrepancies between strips due to attitude and position errors in the inertial motion unit, and combine corrections in order to minimize both relative and absolute error. This method uses a rigorous time-dependent approach to address effects such as IMU drifts and oscillations, which cannot be corrected with classical sensor calibrations.

The technique corrected the trajectory (position, attitude, depth) of the sensor rather than a 'rubber-sheet' best fit of surfaces. This ensured the systematic errors in multibeam surveys were reduced at the source of the error rather than the output data. The output of GGMatch was a series of adjusted trajectory files and a series of adjusted LAZ files, which were then

processed in BathyQC to generate the final data output. The xyz data were gridded for export at 50 cm and 25 cm resolutions.

We compared key bathymetric features against the SSS data (see below), and vice versa, by coplotting bathymetric and SSS data in SonarWiz 7. The gridded MBES data were inspected throughout the study area, with an example plotted in Figure 1D. Here, we reproduce this plot at a larger scale in Figure S7A, as well as providing more detailed image panels that match the areas of interest shown in Figure S7A. This figure provides insight into the detailed topographic structure of the bedrock features in the zoomed AOIs, as well as the transition to the large dune fields towards the left bank of the channel.

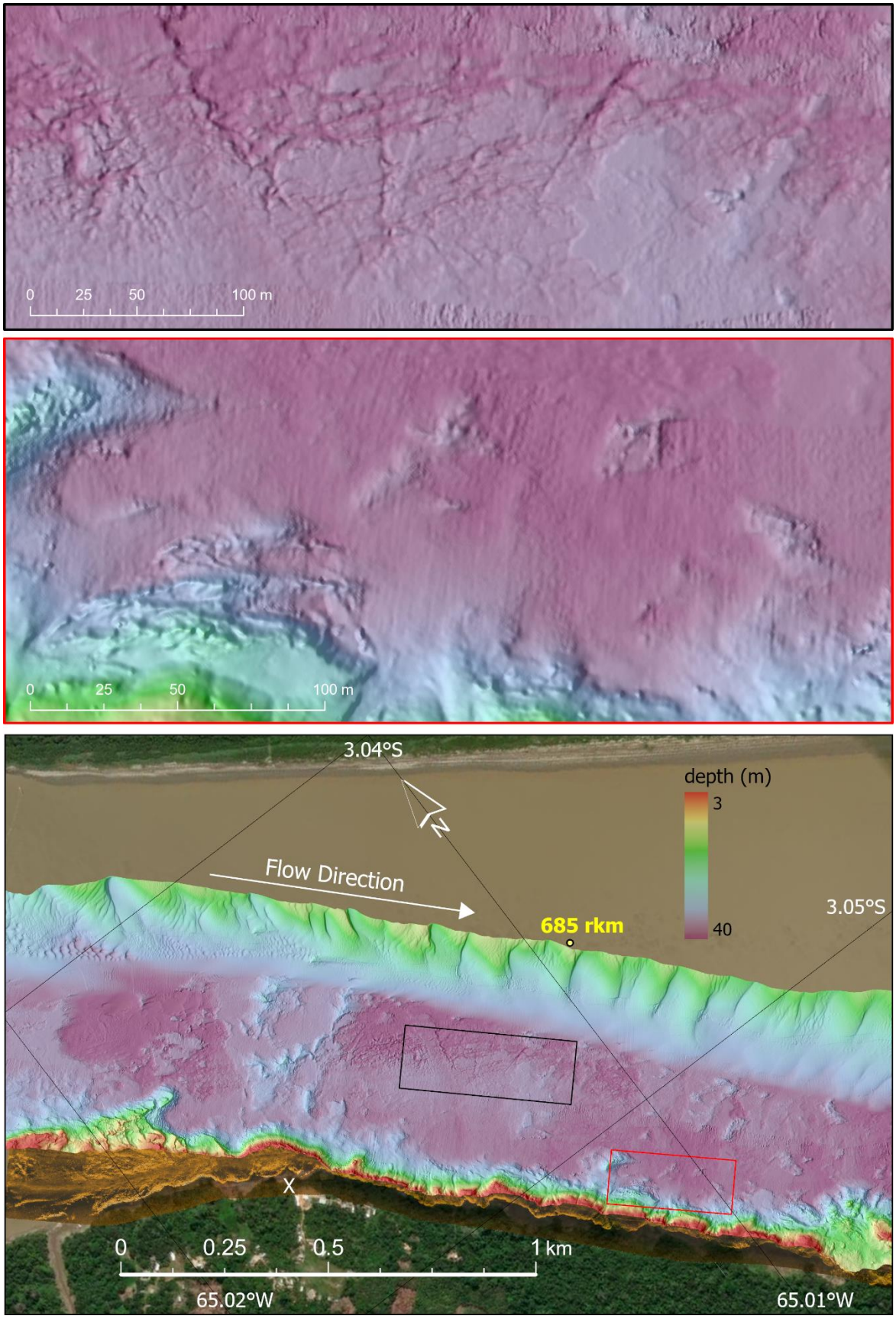


**Figure S7A.** MBES Sonar data for the same AOIs depicted in Figure 1D, with SSS along the right bank (fully presented in S7B). Depths indicated by color, overlying a surface shaded to illustrate texture. Close up of regions in black and red shown in the upper and middle plots respectively.

4.2 Side-Scan Sonar

Survey swaths were collected along ~110 km of the Solimões River using a custom TriTech ROV side-scan sonar (SSS) unit mounted to a bespoke 'river fish' that was pole-mounted using a swing arm to a small sonar vessel. This 450kHz CHIRP system has a 0.5° horizontal beam width and a 60° vertical beam width that can be angled for optimal performance for bankline surveys, and was typically run at 100 m swath range per channel, with a distance accuracy of approximately 5 mm. A Trimble ProXRT was mounted to the top of the sonar pole, with OmniSTAR G2 service including complete GLONASS correction data in the solution, providing sub-decimeter real-time positioning for survey lines. An inertial compass was also used for some of the surveys. Attention was paid to maximize beam performance for the particular vessel and river, including isolation from all motor and electrical noise.

Surveys were managed and data collected using SonarWiz 7, which provides real-time processing and display of results. The configuration allows surveying of water as shallow as 1 meter, with the spring-loaded swing arm and sensor resilient against impacts from logs and rocks. The system provides high resolution depth data under the boat, XY planform location for the bright return at the bank waterline, and a high-resolution backscatter image everywhere else. This survey boat specifically supported the team measuring bank strength, so was able to collect detailed bedform data near every bank strength measurement site.

Importantly, these surveys provided an extensive map of bathymetric and textural details throughout our study area, informing an optimal strategy for the later MBES surveys. Therefore, the MBES data overlapped with SSS in many places, and we were able to confirm that the match between features was excellent, with a greater spatial coverage provided by the SSS. The SSS image detail is better than 5cm resolution in most locations – varying with distance to the sensor – with brightness reflecting both texture and bed surface inclination.

After the fieldwork was completed, the SSS data were cleaned, gain-normalized, and gridded at key locations at 10 cm resolution (half the typical resolution) for various AOI rectangles using SonarWiz 7, by combining both the side-scan and bathymetry analytical features. Here, Figure S7B presents the SSS dataset AOI rectangle for the same area covered as the MBES data (Figure S7A), along with two zoomed images of specific areas that illustrate the prevalence of exposed bedrock without any overlying bed material deposits. For Figures 1D and S7A (lower panel), we present the SSS data as a narrow bronze strip along the right bank waterline, a region without MBES data. It should be noted that these images were collected during low flow stage, when one might expect more extensive bed material deposits due to the much lower bed shear stress present during lower flows.

For SSS images, return energy is depicted in a shaded bronze color. Brighter returns indicate: 1) surfaces inclined perpendicular to the sonar; 2) surfaces composed of rougher sand that reflects sonar energy efficiently, and/or, 3) a hard reflection off the right bank waterline. Darker returns indicate: 1) surfaces inclined away from the sonar (e.g., reflecting energy away), and/or 2) surfaces composed of finer, clay-rich deposits. Swath-parallel 'seams' correspond either to nadir returns (blurry) or the stitching between two swath passes (slightly hatched zones farther from the nadir seams).

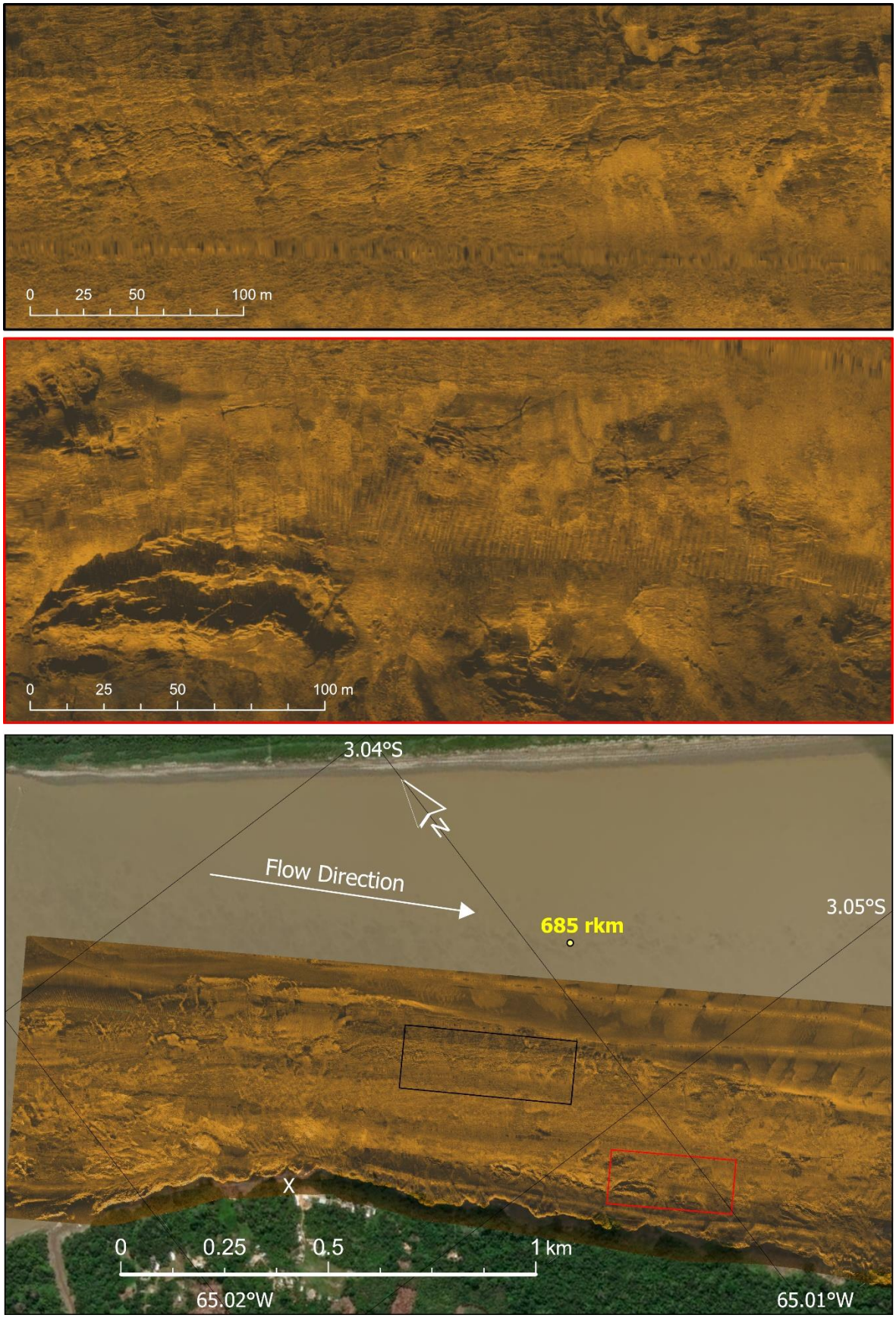


**Figure S7B.** Side-Scan Sonar data for the same AOI depicted in Figure 1D. Zoom images, located by box color, depict bedrock texture, not sandy bed deposits, along with several submerged tree boles. The white X represents a location where bank strength measurements were taken just above the waterline.

## References


Birkett, C. M. , L. A. K. Mertes, T. Dunne, M. H. Costa, and M. J. Jasinski. (2002). Surface water dynamics in the Amazon Basin: Application of satellite radar altimetry. *J. Geophysical Research, 107(D20)*, doi:10.1029/2001JD000609

Dunne, T., Mertes, L. A. K., Meade, R. H., Richey, J. E., & Forsberg, B. R. (1998). Exchanges of sediment between the flood plain and channel of the Amazon River in Brazil. *Bulletin of the Geological Society of America*, *110*(4), 450–467. https://doi.org/10.1130/0016-7606(1998)110<0450:EOSBTF>2.3.CO;2

Hawker, L., Uhe, P., Paulo, L., Sosa, J., Savage, J., Sampson, C., & Neal, J. (2022). A 30 m global map of elevation with forests and buildings removed. *Environmental Research Letters*, *17*(2). https://doi.org/10.1088/1748-9326/ac4d4f

He, C., You, Y., Wang, D., & Wu, H. (2018). Estimating soil failure due to torsion via vane shear test by varying vane diameter and soil properties. *Soil and Tillage Research*, *177*, 68–78. https://doi.org/10.1016/j.still.2017.12.004

Jafari, N. H., Harris, B. D., Cadigan, J. A., Day, J. W., Sasser, C. E., Kemp, G. P., Wigand, C., Freeman, A., Sharp, L. A., Pahl, J., Shaffer, G. P., Holm, G. O., & Lane, R. R. (2019). Wetland shear strength with emphasis on the impact of nutrients, sediments, and sea level rise. *Estuarine, Coastal and Shelf Science*, *229*. https://doi.org/10.1016/j.ecss.2019.106394

Mertes, L. A. K., & Dunne, T. (2022). Effects of Tectonism and Sea-Level Change on the Form and Behaviour of the Modern Amazon River and Its Floodplain. *Large Rivers: Geomorphology and Management, Second Edition*, 171–204.

Mertes, L. A. K., Dunne, T., & Martinelli, L. A. (1996). Channel-floodplain geomorphology along the Solimões-Amazon River. *GSA Bulletin*, *108*(9), 1089–1107. https://doi.org/doi: https://doi.org/10.1130/0016-7606(1996)108<1089:CFGATS>2.3.CO;2

Pekel, J. F., Cottam, A., Gorelick, N., & Belward, A. S. (2016). High-resolution mapping of global surface water and its long-term changes. *Nature*, *540*(7633), 418–422. https://doi.org/10.1038/nature20584

Scherer, D. , C. Schwatke , D. Dettmering , F. Seitz. (2022). ICESat-2 Based River Surface Slope and Its Impact on Water Level Time Series From Satellite Altimetry. Water Resources Research, *58.* https://doi.org/10.1029/2022WR032842

Schwenk, J., Khandelwal, A., Fratkin, M., Kumar, V., & Foufoula-Georgiou, E. (2017). High spatiotemporal resolution of river planform dynamics from landsat: The rivMAP toolbox and results from the Ucayali river. *Earth and Space Science*, *4*(2), 46–75. https://doi.org/10.1002/2016EA000196

Toivonen, T., Mäki, S., & Kalliola, R. (2007). The riverscape of Western Amazonia - A quantitative approach to the fluvial biogeography of the region. *Journal of Biogeography*, *34*(8), 1374–1387. https://doi.org/10.1111/j.1365-2699.2007.01741.x

Tolhurst, T. J., Black, K. S., Shayler, S. A., Mather, S., Black, I., Baker, K., & Paterson, D. M. (1999). Measuring the in situ Erosion Shear Stress of Intertidal Sediments with the Cohesive Strength Meter (CSM). *Estuarine, Coastal and Shelf Science*, *49*, 281–294. https://doi.org/https://doi.org/10.1006/ecss.1999.0512

Vardy, S., Saunders, J. E., Tolhurst, T. J., Davies, P. A., & Paterson, D. M. (2007). Calibration of the high-pressure cohesive strength meter (CSM). *Continental Shelf Research*, *27*(8), 1190–1199. https://doi.org/10.1016/j.csr.2006.01.022

Widdows, J., Friend, P. L., Bale, A. J., Brinsley, M. D., Pope, N. D., & Thompson, C. E. L. (2007). Inter-comparison between five devices for determining erodibility of intertidal sediments. *Continental Shelf Research*, *27*(8), 1174–1189. https://doi.org/10.1016/j.csr.2005.10.006